Published in final edited form as:
Magn Reson Med. 2012 February ; 67(2): 344–352. doi:10.1002/mrm.23007.

Temporal SNR Characteristics in Segmented 3D-EPI at 7T

W. van der Zwaag[1,2,*], **J. P. Marques**[1,2], **T. Kober**[1], **G. Glover**[3], **R. Gruetter**[1,2,4], and **G. Krueger**[5]

[1]Laboratory for Functional and Metabolic Imaging, Ecole Polytechnique Fédérale de Lausanne, Switzerland [2]Radiology, University of Lausanne, Switzerland [3]Radiological Sciences Laboratory, Stanford University, Stanford, CA, USA [4]Radiology, University of Geneve, Switzerland [5]Siemens Schweiz AG, Healthcare Sector IM&WS S, Renens, Switzerland

Abstract

Three-dimensional segmented echo planar imaging (3D-EPI) is a promising approach for high-resolution functional magnetic resonance imaging, as it provides an increased signal-to-noise ratio (SNR) at similar temporal resolution to traditional multislice 2D-EPI readouts. Recently, the 3D-EPI technique has become more frequently used and it is important to better understand its implications for fMRI. In this study, the temporal SNR characteristics of 3D-EPI with varying numbers of segments are studied. It is shown that, in humans, the temporal variance increases with the number of segments used to form the EPI acquisition and that for segmented acquisitions, the maximum available temporal SNR is reduced compared to single shot acquisitions. This reduction with increased segmentation is not found in phantom data and thus likely due to physiological processes. When operating in the thermal noise dominated regime, fMRI experiments with a motor task revealed that the 3D variant outperforms the 2D-EPI in terms of temporal SNR and sensitivity to detect activated brain regions. Thus, the theoretical SNR advantage of a segmented 3D-EPI sequence for fMRI only exists in a low SNR situation. However, other advantages of 3D-EPI, such as the application of parallel imaging techniques in two dimensions and the low specific absorption rate requirements, may encourage the use of the 3D-EPI sequence for fMRI in situations with higher SNR.

Keywords

3D-EPI; EVI; tSNR; SNR

INTRODUCTION

Echo Volumar Imaging (1,2) has recently become a method of interest for fMRI (3,4), primarily because of the potential high temporal resolution. However, there are other motivations to employ 3D methods for fMRI rather than the conventional 2D multislice approach: a higher sensitivity per unit scan time (5,6), the absence of a spin-history artefact (7) and the possibility of applying parallel imaging techniques in two dimensions (8).

However, 3D single-shot acquisitions require long echo trains, which require compromises in terms of minimum achievable echo time (TE) and spatial resolution or very high demands on the gradient hardware (4). To overcome those limitations, recent investigations focused

[*]Correspondence to: W. van der Zwaag, Ph.D., LIFMET, EPFL, Station 6, CH-1015 Lausanne, Switzerland. wietske.vanderzwaag@epfl.ch.

on the use of outer volume suppression (9), the use of surface coils to restrict the actual field-of-view (2,4,6) or high parallel imaging factors to reduce the number of phase-encoding steps (3,8,10,11). Another strategy to overcome the limits is the acquisition of the 3D volume in several shots (7,12,13). In this case, temporal resolution is reduced to TR times the number of segments. However, individual read-out trains are shorter than in a 3D single-shot approach, thereby allowing acquisitions with

at high magnetic fields. This segmented three-dimensional echo planar imaging (3D-EPI) has been shown to be advantageous for fMRI (14,15).

The optimum excitation flip angle (Ernst angle: $\alpha_{Ernst} = \text{acos}(\exp(-TR/T_1))$) is significantly reduced for 3D-EPI compared with the 2D-EPI since a much shorter TR is used. In particular at high magnetic fields, the use of volume excitation with a small flip angle may become beneficial as it is much less specific absorption rate (SAR) intensive than the sequential excitation of a series of thin slices with a larger flip angle. Especially when fat-suppression is added to the EPI acquisition, SAR limits pose a problem in high field fMRI acquisitions (16) and this SAR load can be drastically reduced by moving from 2D to segmented 3D approaches.

Even though a small flip angle is typically used for volume excitation in segmented 3D-EPI, a higher signal-to-noise ratio (SNR) is reached in 3D EPI than in multi-slice 2D EPI acquired using a large flip angle (12,14). Moreover, the SNR in the short-TR regime is less sensitive to B_1-inhomogeneity common at ultra-high field than the long-TR regime employing large flip angles.

The use of segmented, or multishot, 3D-EPI has been suggested especially for use at ultra-high field (≥7T) (14), where the stronger signal is used to image at higher spatial resolution. In whole-brain 2D multislice fMRI experiments in humans with high spatial resolution (~1 mm^3), the temporal resolution is limited by the acquisition of numerous (>75) thin slices within a certain repetition time, TR. A segmented 3D acquisition allows under-sampling (parallel imaging acceleration) in the slice-select direction, leading to a reduction in the minimum available volume TR by 1/acceleration factor (14). Other techniques which allow acceleration in the slice-selection direction, such as those based on a GRASE readout (8) or CAIPIRINHA (17,18) are more SAR intensive and thus less straightforward to use at higher fields. The same holds true for spatial multiplexing-EPI, which allows accelerations of 4 and above at the cost of increased SAR requirements (19). Keyhole-type acquisitions have also been suggested for fMRI (20), but the increased spatio-temporal resolution here comes at the cost of an increased temporal auto-correlation and thus a significant statistical bias.

Noteworthy, a potential disadvantage of segmented volume acquisitions is the increased temporal signal variation, which has been reported for segmented 3D techniques compared with 2D multislice acquisitions (5,12,14,15). This may affect the results of fMRI studies significantly.

While 3D-EPI has been used for fMRI studies successfully in comparison with 2D EPI, the effects of changing the number of segments are not well understood. In this study, we specifically investigate the temporal signal properties of segmented 3D EPI approaches. In phantom and in vivo experiments, λ, an SNR system property (21), is measured as a function of the number of *k*-space planes/segments in segmented 3D-EPI resting state data to characterise the temporal noise characteristics of the segmented 3D-EPI sequence. Signal strength was varied by varying spatial resolution. In addition, fMRI data was acquired with both the 2D-EPI and 3D-EPI sequences at two different spatial resolutions to demonstrate BOLD sensitivity differences.

THEORY

The comparison of the image SNR, SNR_0, and temporal SNR, tSNR, has been shown to be a good measure for sensitivity to system instabilities and physiological signal variations (21–23). In an ideal system, without any system fluctuations, all points on an SNR_0 – tSNR curve would fall on a line through unity. Temporal signal fluctuations may arise from system instability or physiological processes, leading to an asymptotic limit of tSNR over SNR_0.

The relationship between tSNR and image SNR_0 is given by Eq. 1 (23):

$$\mathrm{tSNR}=\frac{\mathrm{SNR}_0}{\sqrt{1+\lambda^2+\mathrm{SNR}_0^2}} \quad [1]$$

where λ is a system dependent constant. λ demonstrates a physical measure of the SNR-degradation by signal-dependent fluctuations, such that if λ = 0, tSNR = SNR_0. For large values of SNR_0, tSNR = λ^{-1}. Thermal and physiological noise contributions are equal when SNR0 = λ^{-1} and this point has been suggested as the optimum voxel size for fMRI (24). λ can be measured by varying the signal strength, e.g. through changes in flip-angle, spatial resolution, TE or field strength (22).

A more detailed analysis has shown that λ can be described using Eq. 2 (21):

$$\lambda^2=c_1^2\cdot\Delta R_2^{*2}\cdot\mathrm{TE}^2+c_2^2 \quad [2]$$

where c_1 is a constant describing the BOLD-like, TE dependent, signal fluctuations and c_2 reflects the contribution of the non-TE dependent noise sources.

METHODS

Data Acquisition

All experiments were conducted according to the procedure approved by the institutional review board and all participants provided written informed consent before the experiments. Nine healthy subjects (6 males, 3 female, average age 30.5 years) were scanned on a 7T/ 680 cm head-only scanner (Magnetom 7T, Siemens, Erlangen, Germany) equipped with a head gradient insert (80 mT/m maximum gradient strength, 333 T/m/s max slewrate).

An 8-channel rf-head coil (Rapid Biomedical, Wurzburg, Germany) was used for rf-transmission and reception. Phantom experiments were repeated using a cp-head coil (InVivo, Peewaukee, WI) for rf-transmission and reception.

A gradient-spoiled segmented 3D-EPI sequence was used for all data acquisitions (14). In this implementation, one segment equals the acquisition of one *k*-space plane. A seven-lobe sinc pulse was used for volume excitation. To avoid build-up of spurious echos, spoiler gradients were applied on all three gradient axes.

For five subjects, sixteen resting state fMRI datasets with different spatial resolutions and/or segments were acquired per subject in one imaging session. The number of segments and the in-plane resolution were stepped through as shown in Table 1. In-plane resolutions were chosen so that the volume of the voxel changed roughly by a factor 2 between the different resolutions.

For each resting state fMRI dataset, a series of 50 imaging volumes was acquired ($TR_{segment}$/TE/flip angle = 150ms/ 28 ms/23°, BW_{ro} = 1410 Hz/pixel, GRAPPA = 2) with anterior-posterior phase-encoding direction. Slice thickness was 2 mm for all acquisitions. In the case of 1 segment (i.e. the 2D-EPI case), 3 slices were acquired per 150 ms to allow for 6-parameter rigid-body motion correction.

Identical experiments were also performed on a 13-cm diameter spherical phantom filled with oil. Finally, phantom experiments were repeated using the cp-head coil without application of parallel imaging, using a modified range of voxel sizes as shown in Table 1. $TR_{segment}$, TE and flip angle were the same as in the previous experiments, while the bandwidth was changed to 2604 Hz/pixel.

Four subjects participated in the motor-task fMRI experiments. Each subject underwent four runs of the same visually cued bilateral fingertapping protocol (12 s tapping, 18s rest, 6 repetitions). Two datasets were acquired using 2D-EPI, both with 16 slices per volume, once with 1 mm isotropic voxels and once with 3 mm isotropic voxels. The other two datasets were acquired using 3D-EPI with 16 segments and the same spatial resolutions as for the 2D-EPI. Other parameters were: $TR_{segment}$/TE/flip angle = 150ms/27ms/23° for the 3D data, resulting in a TR_{volume} of 2400 ms and TR/TE/flip angle = 2400ms/ 27ms/75° for the 2D data. Where the flip angle was limited by the SAR in the 2D case, the largest flip angle allowed by the SAR monitor was used. Further, matrix size = 128 × 128, BW_{ro} = 1860 Hz/pixel and GRAPPA = 2 for the 1 mm isotropic data and matrix size 64 × 64 and BW_{ro} = 1660 Hz/pixel for 3 mm data. Runs were counterbalanced across subjects.

Data Analysis

Data from separate coil elements of the 8-channel rf-coil were recombined using the sum-of-squares method. *In-vivo* data were motion corrected using FLIRT in FSL (25). Displacement was <1.5 mm for all subjects and all data were used for further processing.

For all human images, SNR_0 and tSNR were determined in manually drawn regions of interest (ROIs) in occipital grey matter, parietal white matter and in the cerebrospinal fluid (CSF) in the ventricles. ROIs were drawn on the 1.5 mm in-plane resolution data, which had sufficiently high CNR to distinguish grey and white matter reliably. To allow the ROIs to be in the same location in all datasets for a given subject, the ROIs were positioned in the centre slices of the 2D-EPI. In the phantom images, SNR_0 and tSNR were evaluated in a 25-voxel square ROI placed in the middle of the image.

tSNR was measured as the temporal mean value of an ROI, divided by the temporal standard deviation. The SNR_0 was calculated as described by Constantinides et al. (26), including corrections for noise bias effects. Since the plots provided in (26) only extend to 4 array elements the graph for the 8-channel case was first generated as described in (26) and SNR_0 values were corrected using the new curve.

To fully equate SNR_0 and tSNR, further scaling factors are necessary (27) which were here obtained from a fit of Eq. 1 to the phantom data, using $SNR_0 = b \times SNR'$, where b is the scaling factor (here 0.47) and SNR' the in-plane SNR prior to scaling. Human SNR_0 values were corrected using the obtained b factor. Values for λ were then obtained from a nonlinear least-squares fit in Matlab (the Mathworks) to Eq. 1.

Motor-task fMRI data were analysed using FEAT from FSL (www.fmrib.ox.ac.uk/fsl) including motion correction, spatial smoothing with a Gaussian of full width at half maximum 1.5 mm for the 1 mm data and full width at half maximum 5 mm for the 3 mm data and highpass temporal filtering (σ = 50 s). Time series analysis was carried out using

FILM with local autocorrelation correction (28). Activation maps were thresholded at $Z > 2.3$ and a corrected cluster threshold of $P = 0.05$. The number of activated voxels was measured in the centre 12 slices as well as the mean z-score in an ROI covering both motor cortices. The ROI was moved between datasets by applying co-registration parameters obtained from a registration between runs (6 parameter rigid-body), without re-slicing of the functional data. SNR and tSNR values calculated as described above were obtained from a parietal region not displaying any activation, containing predominantly gray matter. Relative differences within subject in SNR values, numbers of active voxels and mean z-scores between 2D and 3D data were tested via one-tailed t-tests ($n = 4$) in Matlab.

RESULTS

For both rf-coils, phantom data confirmed a linear relationship between voxel size and SNR_0 for all numbers of segments acquired (Fig. 1a,b). Also, all data-points fell along very similar SNR_0 – tSNR curves for both 8-channel coil and CP-coil data (Fig. 1c,d). A plateau is not really reached, presumably because SNR_0 values were not sufficiently high to sample the curve in the graph adequately. Values for λ of 0.0016 ± 0.0004 (estimated value ± 95% confidence interval) and 0.002 ± 0.001 were found for the 8-channel coil and CP coil respectively from a fit to Eq. 1. The results of the fits are displayed in Fig. 1 with continuous lines. Separate fits of Eq. 1 for the data series with different numbers of segments did not result in significantly different values of λ.

An example of a 32-segment human dataset acquired with the 3D-EPI sequence is shown in Fig. 2. The quality of the slab profile obtained with the seven-lobe sinc pulse in the H-F direction can be judged from the sagittal and coronal orientations, where only the most outer slices are visibly affected. Typical 2D EPI data exhibit significant signal distortions and voids in the frontal lobe area, which are greatly reduced in the present segmented 3D-EPI data. In-plane distortions are identical to those seen in multislice echo planar images because the read-out echo train length per segment is the same as that of a 2D multislice acquisition. On the other hand, the gradient responsible for the through-slice dephasing in the 2D EPI experiments causes a distortion in the slice direction in the 3D-EPI acquisition.

On average, over subjects, number of segments and tissue type, SNR_0 increased linearly with voxel size (linear regression, R = 0.998). SNR_0 in the 8, 16, and 32 segment data, increased on average, over subjects, tissue types and voxel sizes, by 180, 300, and 440 % relative to the single shot data because of the longer total acquisition time employed for the multisegment data. This increase was linear with the square root of the number of segments, and thus acquisition time ($R = 0.998$).

Graphs presenting tSNR vs. SNR_0 values in ROIs in grey and white matter and CSF are shown in Fig. 3. For a given SNR_0 level, a tSNR decrease with increasing number of segments was observed for all tissue types. Generally, SNR_0 values are highest in CSF and lowest in white matter, in agreement with the contrast in the image shown in Fig. 2. For the tSNR, highest values were found in the CSF and lowest values in grey matter. This is to be expected, as BOLD-type signal fluctuations are expected to appear more prominent in grey matter than in white matter or CSF. Lower values for tSNR in CSF regions have previously been found in ROIs including voxels on the brain surface (24), possibly because those are more sensitive to partial volume effects and subject motion; however, Poser et al found the same trends reported here ($tSNR_{CSF} > tSNR_{white\ matter} > tSNR_{grey\ matter}$) (14).

Values for λ for the 3 tissue types in data acquired with different numbers of segments are given in Table 2. Values for the single segment data of the white and grey matter ROIs are comparable to results presented previously for a 3 T scanner (21). The fit results follow the

trends given by the tSNR values: an increase in λ with number of segments and $\lambda_{GM} > \lambda_{WM} > \lambda_{CSF}$. However, only λ_{32} is significantly different from λ_1 in all three tissue types (two-tailed t-test, $P < 0.05$). Both λ_8 and λ_{16} in white matter and λ_{16} in CSF are also significantly larger than λ_1 (two-tailed t-test, $P < 0.05$).

When plotting values obtained for λ against numbers of segments used in the acquisition, as in Fig. 4, a linear trend ($R^2 > 0.98$) was found for all tissue types. The fits to grey matter, white matter and CSF data points, are shown overlaid on the data in Fig. 4. Slopes found for grey matter, white matter and CSF were 0.0009, 0.0009, and 0.0007, respectively.

fMRI data from a representative subject are shown in Fig. 5. SNR / tSNR values for the 1mm 2D-EPI, 1 mm 3D-EPI, 3mm 2D-EPI and 3 mm 3D-EPI were 7 ± 1/8 ± 1, 9 ± 1/9 ± 1, 146 ± 11/62 ± 3, and 190 ± 20/50 ± 4, respectively (mean over subjects ± stderr). While the SNR was higher for the 16-segments 3D-EPI data at both resolutions ($P < 0.05$), tSNR was higher for the 2D-EPI when an isotropic voxel size of 3 mm was used ($P < 0.05$) and showed a trend for higher values in the 16-segment 3D-EPI data for a voxel size of 1 mm ($P = 0.09$). This is also reflected in the numbers of activated voxels and obtained z-scores, which were not significantly different for the 3mm resolution data, but slightly higher for the 2D-EPI, namely 2774 ± 550 and 2526 ± 360 active voxels (mean over subjects ± stderr, $P = 0.37$) and z-scores of 3.8 ± 0.5 and 3.4 ± 0.5 ($P = 0.26$) for the 2D and 3D data, respectively. However, for the 1 mm resolution case, the results were different: the 3D-EPI data showed a trend towards more activated voxels and higher z-scores than the 2D-EPI: 2539 ± 400 and 3411 ± 650 active voxels (mean over subjects ± stderr, $P = 0.09$) and z-scores of 1.1 ± 0.1 and 1.8 ± 0.2 ($P = 0.06$) for the 2D and 3D data, respectively. Mean z-score values were quite low as the ROIs covered a relatively large area (see also Fig. 5).

DISCUSSION

Acquisition

The $TR_{segment}$ in the resting state experiments was kept constant to allow a comparison between the data with different numbers of segments with the same T_1-weighting. Compared to a ‘standard’ multislice acquisition with onger TR and large flip angle, the SNR_0 in the present 1-segment data is consequently reduced. However, this is of no influence on the measurement of λ, as datasets with different SNR levels fall on the same SNR_0 – tSNR curve (22) and so the only prerequisite for a good measurement of λ is the spread of SNR_0 – tSNR points along the curve.

Equally, the used GRAPPA factor of 2 for the 8-channel coil data causes a reduction in SNR, but no change in λ, as λ depends on signal strength, which is not affected in an accelerated experiment (29). To further avoid a bias of the data due to the use of parallel imaging, all datasets here were acquired with an identical speed-up factor of 2, so that any effects would be identical across datasets. Moreover, experiments were repeated for the phantom with a single channel CP-head coil, which yielded lower SNR_0 and tSNR values at the same spatial resolution, but no significant difference in the measurement of λ.

The slab thickness varied with the number of segments to keep the slice-thickness constant at 2 mm. It could be argued that in the 1-segment data, the slice of interest may thus be affected by an imperfect slice selection profile, while this is not the case in the centre slices of multi-segment acquisitions. However, it is assumed that this has no influence on the measurement of λ and that the result of slice-selection imperfections on the 1-segment curve is a shift of the points towards lower SNR values along the λ curve.

The 8-segment 3D-EPI also has an imperfect point-spread function in the slice-select dimension, because of the spatial interference caused by sampling a small number of points in the k_z direction (30). Similarly, since this affects all scans with the same number of segments in the same way, no influence on the measurement of λ is expected.

Because of the larger imaging matrix, the total read-out duration for the 1.5 mm in-plane resolution datasets was 11% longer than that of the other datasets, irrespective of the number of segments. This may have led to a small increase of the local point spread function (31), which was not taken further into account as motion correction in the case of human data and indeed averaging over an ROI were assumed to introduce larger amounts of spatial smoothing.

All segmented 3D-EPI resting state experiments were acquired with the same range of spatial resolutions. This resulted in very high SNR_0 measurements for the 16-segment and 32-segment datasets, such that almost all tSNR vs SNR_0 measurements were on the plateau of the curve. Exclusively sampling the plateau does not allow for a good-quality fit and thus the 95% confidence ranges found on the multisegment data are larger than those of the fits to 1-segment or 8-segment data.

Phantom Results

In the phantom experiments, without any physiological contributions to the noise, increases in SNR_0 for data with larger numbers of segments were accompanied with increases in tSNR as described by Eq. 1 (Fig. 1c,d). Because no time-dependent processes, other than hardware-related signal drifts and fluctuations, occur in the phantom, the longer acquisition window results in higher temporal SNR. This confirms that the trends seen in the human data are due to signal fluctuations arising from physiological processes. The values for lambda obtained here are comparable to values of 0.0008 and 0.002 previously reported for a 7T (22) and a 3T scanner (21), respectively, suggesting comparable hardware-related signal drifts between systems.

Human Results

Previously, incomplete transverse relaxation between excitation pulses has been suggested as a source of signal fluctuations in 3D-EPI (12). However, the spoiler gradients played out after the acquisition train destroy any remaining residual transverse magnetisation. Therefore, incomplete transverse relaxation between excitation pulses is unlikely to be the cause of the reduced tSNR seen with higher numbers of segment acquired. Furthermore, at 7 Tesla, only the T_2 of CSF is not significantly shorter than TR and the tSNR in CSF is consistently higher than in both grey and white matter.

Similarly, in-flow effects could be different between acquisitions with different numbers of segments as the size of the excited slab is dependent on the number of segments acquired per volume. A relatively small flip angle of 22 degrees was used for all excitations to minimize T_1 contrast between inflowing and stationary spins, but at the short TR of 150 ms used here T_1-weighting is still expected. If variations in T_1-weighting of the inflowing spins would be a significant factor in the temporal stability of the signal, then it should be expected that the tSNR in the thinner slabs, with less segments, would be most affected because of the shorter edge-ROI distances and thus an decreasing value of λ would be found with increasing numbers of segments. As this is not the case, it seems that the different size of excited slab is not a significant factor in the tSNR measurements. Also, we evaluated only the centre slice, further reducing the potential inflow effects.

The large difference in signal stability in human and phantom data is understood to be dominated by respiratory or cardiac fluctuations, but also partially caused by bold-like signal

fluctuations. In the data acquired here, these signal fluctuations may reflect variations in resting state networks when no active task was demanded of the subjects. It is not known how much of the signal variance is caused by bold-like signal fluctuations and how much is caused by non bold-like signal fluctuations. A multiecho acquisition could be used to clarify this via the TE dependence of the noise and the determination of the c_1 and c_2 constants in Eq. 2. (21).

The variation of λ with number of segments in the acquisition could be incorporated in the model by expanding Eq. 1. As the phantom data do not show the same trend as the human data, the variation in lambda is assumed to be caused by a shot-to-shot phase variation due to physiological processes and, therefore, to be TE dependent. Therefore, a segment-dependence of c_1 should be included, but the current study does not allow further specification of this dependence. An expansion of the model is also appropriate because of the relatively poor quality of the fits to the multi-segment data.

Motor Task fMRI

The fMRI experiments including a simple motor task confirm the results of the SNR/tSNR measurements in resting state data. When 16 segments are used in the 3D-EPI sequence, at 3mm spatial resolution and SNR values around 150, the tSNR (See Fig. 3A), and BOLD sensitivity is higher in an equivalent 2D-EPI sequence with equal brain coverage and acquisition time per volume, which results in a slight trend towards higher mean z-score and number of active voxels in the 2D-EPI. However, if the spatial resolution is increased in both sequences, the increase in in-plane SNR in the 3D-EPI relative to the 2D-EPI does translate in higher tSNR and stronger trends of higher z-scores and extent of activation in the 3D-EPI data. The SNR increase here is not linear with the square root of the number of *k*-space planes, as in the resting state data, because the TR of the 2D-EPI was much longer than the $TR_{segment}$ of the 3D-EPI, to allow a real-life comparison between the two sequences. The SNR_0 values in the 1 mm datasets were fairly low, below the suggested point of SNR = $1/\lambda$ (24), but comparable acquisitions using array coils with larger numbers of receivers would yield higher SNR_0 values.

These experiments confirm that 3D-EPI will be beneficial for fMRI when scanning in a thermal noise-dominated regime. Additionally, some benefit may be expected for functional experiments that do not require such high spatial resolutions, from acquiring high resolution data followed by spatial smoothing, as suggested by Triantafyllou et al (32). Another approach would be the removal of the physiological signal components through RETROICOR or related methods, which has shown benefits in 3D-EPI (33).

Effect of Segments on Acquisition Parameters

From Fig. 3, it can be seen that for the right-most points in each series, at SNR_0 values of 150 or higher, tSNR decreased with increasing numbers of segments. However, for lower SNR_0 values this is not the case. In the left-most data-points from each series, corresponding to a resolution of 1.5*1.5*2 mm and at SNR_0 values below 100, the 8-segment dataset yielded highest tSNR values and the 1-segment dataset yielded lowest tSNR values. It is to be expected that at even lower SNR_0 levels even higher numbers of segments will yield highest tSNR levels as the large thermal noise contribution at such high resolutions allows profiting from the increased SNR available due to the increased number of *k*-space planes sampled. The smaller the voxel size, and thus lower the SNR_0, the more segments can be used to cover a whole brain while working in a thermal-noise dominated regime. It should be noted that increases in SNR_0, for example through the use of better rf-coils would shift all the points rightwards along the curves (27) relative to the data presented in Fig. 3.

Thus, the SNR advantage of a segmented 3D-EPI sequence for fMRI exists only when working in a thermal-noise dominated regime. However, the other advantages of 3D-EPI, namely low SAR values, the possibility of applying parallel imaging techniques in both phase-and slice-encoding directions and the reduced through-slice de-phasing effects may also encourage the use of the 3D-EPI sequence for fMRI in situations with higher SNR_0 levels.

The dependence of the tSNR on the number of segments used for acquisition of a volume of an fMRI data train, as shown by the data presented, is of importance for the selection of acquisition parameters for any fMRI study using segmented 3D-EPI. At lower field strengths, where the physiological component of the noise is less important (22), larger voxels and/or numbers of segments can be used while remaining in a thermal-noise dominated regime. However, at higher fields, to avoid signal-dependent noise becoming dominant over thermal noise, care should be taken to use an appropriate voxel size, as demonstrated in Fig. 3, and number of segments. The latter one could be controlled via high parallel imaging speed-up factors in the slice encoding direction and/or sampling of multiple k-space planes per excitation, which would also aid to achieve good brain coverage while using thin slices. Lambda, and thus the optimal SNR_0 level (24), can be estimated from the data presented in Fig. 4.

CONCLUSION

3D-EPI applied to fMRI offers advantages such as higher SNR and lower SAR values than comparable multislice 2D-EPI as well as the possibility of applying parallel imaging techniques in two dimensions. However, in fMRI, the benefit of higher SNR is only accessible when the data are acquired in a regime where the noise is dominated by thermal, not physiological signal fluctuations. Here, it is shown that the parameter λ, which describes the SNR_0 - tSNR curve, depends on the number of segments in a linear fashion, influencing the optimum scan parameters: increasing numbers of segments, as may be necessary to obtain whole-brain coverage, reduces tSNR, but less so for smaller voxel sizes. Indeed, fMRI data employing a simple-motor task showed a trend toward superior BOLD sensitivity in 3D-EPI for a small voxel size and thus low SNR levels. In conclusion, three-dimensional EPI is a promising method for fMRI when working in a thermal-noise dominated regime.

Acknowledgments

This work was supported by the Centre d'Imagerie BioMédicale (CIBM) of the University of Lausanne (UNIL), the Swiss Federal Institute of Technology Lausanne (EPFL), the University of Geneva (UniGe), the Centre Hospitalier Universitaire Vaudois (CHUV), the Hôpitaux Universitaires de Genève (HUG) and the Leenaards and the Jeantet Foundations and by a Swiss National Science Foundation grant to R. Gruetter.

References

1. Mansfield P, Coxon R, Hykin J. Echo-volumar imaging (EVI) of the brain at 3. 0 T: first normal volunteer and functional imaging results. J Comput Assist Tomogr. 1995; 19:847–852. [PubMed: 8537514]
2. Yang Y, Mattay VS, Weinberger DR, Frank JA, Duyn JH. Localized echo-volume imaging methods for functional MRI. J Magn Reson Imaging. 1997; 7:371–375. [PubMed: 9090593]
3. Rabrait C, Ciuciu P, Ribes A, Poupon C, Le Roux P, Dehaine-Lam-bertz G, Le Bihan D, Lethimonnier F. High temporal resolution functional MRI using parallel echo volumar imaging. J Magn Reson Imaging. 2008; 27:744–753. [PubMed: 18383267]
4. van der Zwaag W, Francis S, Bowtell R. Improved echo volumar imaging (EVI) for functional MRI. Magn Reson Med. 2006; 56:1320–1327. [PubMed: 17089364]

5. Lai S, Glover GH. Three-dimensional spiral fMRI technique: a comparison with 2D spiral acquisition. Magn Reson Med. 1998; 39:68–78. [PubMed: 9438439]
6. Hu Y, Glover GH. Three-dimensional spiral technique for high-resolution functional MRI. Magn Reson Med. 2007; 58:947–951. [PubMed: 17969117]
7. Muftuler LT, Nalcioglu O. Improvement of temporal resolution in fMRI using slice phase encode reordered 3D EPI. Magn Reson Med. 2000; 44:485–490. [PubMed: 10975903]
8. Neggers SF, Hermans EJ, Ramsey NF. Enhanced sensitivity with fast three-dimensional blood-oxygen-level-dependent functional MRI: comparison of SENSE-PRESTO and 2D-EPI at 3 T. NMR Biomed. 2008; 21:663–676. [PubMed: 18189337]
9. Pfeuffer J, van de Moortele PF, Yacoub E, Shmuel A, Adriany G, Andersen P, Merkle H, Garwood M, Ugurbil K, Hu X. Zoomed functional imaging in the human brain at 7 Tesla with simultaneous high spatial and high temporal resolution. Neuroimage. 2002; 17:272–286. [PubMed: 12482083]
10. Poser BA, Norris DG. 3D single-shot VASO using a maxwell gradient compensated GRASE sequence. Magn Reson Med. 2009; 62:255–262. [PubMed: 19319900]
11. Barth M, Meyer H, Kannengiesser SA, Polimeni JR, Wald LL, Norris DG. T2-weighted 3D fMRI using S2-SSFP at 7 tesla. Magn Reson Med. 2010; 63:1015–1020. [PubMed: 20373402]
12. Goerke U, Moller HE, Norris DG, Schwarzbauer C. A comparison of signal instability in 2D and 3D EPI resting-state fMRI. NMR Biomed. 2005; 18:534–542. [PubMed: 16206130]
13. Abduljalil AM, Aletras AH, Robitaille PM. 3D echo planar imaging: application to the human head. Magn Reson Med. 1995; 34:144–148. [PubMed: 7476071]
14. Poser BA, Koopmans PJ, Witzel T, Wald LL, Barth M. Three dimensional echo-planar imaging at 7 Tesla. Neuroimage. 2010; 51:261–266. [PubMed: 20139009]
15. van der Zwaag, W.; Kober, T.; Marques, J.; Glover, G.; Gruetter, R.; Krueger, G. Comparison of single shot 2D EPI and segmented 3D EVI acquisition for fMRI at 7T. Proceedings of the 17th Annual Meeting of ISMRM; Honolulu, Hawaii, USA. 2009.
16. Speck O, Stadler J, Zaitsev M. High resolution single-shot EPI at 7T. Magma. 2008; 21:73–86. [PubMed: 17973132]
17. Breuer FA, Blaimer M, Heidemann RM, Mueller MF, Griswold MA, Jakob PM. Controlled aliasing in parallel imaging results in higher acceleration (CAIPIRINHA) for multislice imaging. Magn Reson Med. 2005; 53:684–691. [PubMed: 15723404]
18. Setsompop, K.; Gagoski, BA.; Polimeni, JR.; Witzel, T.; Wedeen, VJ.; Wald, LL. Blipped CAIPIRINHA for simultaneous multislice EPI with reduced g-factor penalty. Proceedings of the 18th Annual Meeting of ISMRM; Stockholm, Sweden. 2010.
19. Feinberg DA, Moeller S, Smith SM, Auerbach E, Ramanna S, Glasser MF, Miller KL, Ugurbil K, Yacoub E. Multiplexed echo planar imaging for sub-second whole brain FMRI and fast diffusion imaging. PLoS One. 2010; 5:e15710. [PubMed: 21187930]
20. Gao JH, Xiong J, Lai S, Haacke EM, Woldorff MG, Li J, Fox PT. Improving the temporal resolution of functional MR imaging using keyhole techniques. Magn Reson Med. 1996; 35:854–860. [PubMed: 8744013]
21. Kruger G, Glover GH. Physiological noise in oxygenation-sensitive magnetic resonance imaging. Magn Reson Med. 2001; 46:631–637. [PubMed: 11590638]
22. Triantafyllou C, Hoge RD, Krueger G, Wiggins CJ, Potthast A, Wig-gins GC, Wald LL. Comparison of physiological noise at 1. 5 T, 3 T and 7 T and optimization of fMRI acquisition parameters. Neuro-image. 2005; 26:243–250. [PubMed: 15862224]
23. Kruger G, Kastrup A, Glover GH. Neuroimaging at 1.5 T and 3. 0 T: comparison of oxygenation-sensitive magnetic resonance imaging. Magn Reson Med. 2001; 45:595–604. [PubMed: 11283987]
24. Bodurka J, Ye F, Petridou N, Murphy K, Bandettini PA. Mapping the MRI voxel volume in which thermal noise matches physiological noise—implications for fMRI. Neuroimage. 2007; 34:542–549. [PubMed: 17101280]
25. Jenkinson M, Bannister P, Brady M, Smith S. Improved optimization for the robust and accurate linear registration and motion correction of brain images. Neuroimage. 2002; 17:825–841. [PubMed: 12377157]

26. Constantinides CD, Atalar E, McVeigh ER. Signal-to-noise measurements in magnitude images from NMR phased arrays. Magn Reson Med. 1997; 38:852–857. [PubMed: 9358462]
27. Triantafyllou C, Polimeni JR, Wald LL. Physiological noise and signal-to-noise ratio in fMRI with multichannel array coils. Neuroimage. 2011; 55:597–606. [PubMed: 21167946]
28. Woolrich MW, Ripley BD, Brady M, Smith SM. Temporal autocorrelation in univariate linear modeling of FMRI data. Neuroimage. 2001; 14:1370–1386. [PubMed: 11707093]
29. Triantafyllou, C.; Elschot, M.; Polimeni, JR.; Wald, LL. Physiological Noise in GRAPPA fMRI Time-Series. Proceedings of the 17th Annual Meeting of ISMRM; Honolulu, Hawaii, USA. 2009. p. 249
30. Pohmann R, von Kienlin M. Accurate phosphorus metabolite images of the human heart by 3D acquisition-weighted CSI. Magn Reson Med. 2001; 45:817–826. [PubMed: 11323808]
31. Glover GH, Song L. Self-Navigated Spiral fMRI: Interleaved versus Single-shot. Magn Reson Med. 1998; 39:361–468. [PubMed: 9498591]
32. Triantafyllou C, Hoge RD, Wald LL. Effect of spatial smoothing on physiological noise in high-resolution fMRI. Neuroimage. 2006; 32:551–557. [PubMed: 16815038]
33. Jorge, J.; Figueiredo, P.; van der Zwaag, W.; Narsude, M.; Marques, J. Sources of signal fluctuations in single-shot 2D EPI and segmented 3D EVI acquisitions for fMRI at 7T. Proceedings of the 19th Annual Meeting of ISMRM; Montréal, Canada. 2011.

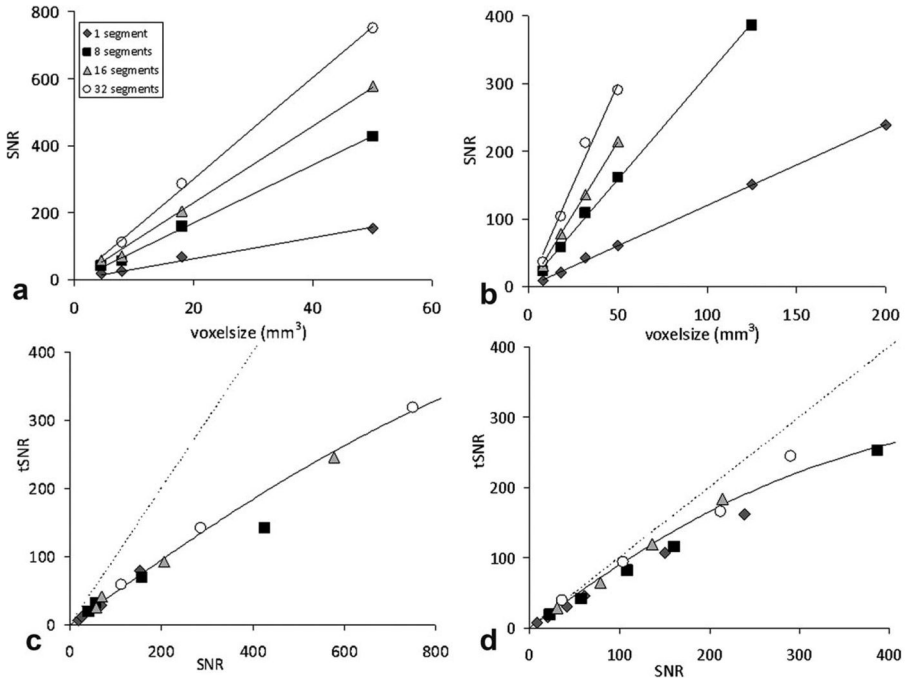

FIG. 1.

Phantom data. **a:** SNR_0 versus voxel size for each of the acquisitions in the 8-channel coil. Continuous lines show the result of linear fits. Note the increase in SNR_0 with number of segments acquired. **b:** SNR_0 versus voxel size for each of the acquisitions in the CP coil. **c:** tSNR versus SNR_0 in phantom data for 1, 8, 16, and 32 segment data acquired using an 8-channel coil. The dotted line indicates unity; the continuous line is the result of a fit to Eq. 1. **d:** tSNR versus SNR_0 in phantom data for 1, 8, 16, and 32 segment data acquired using the CP coil. The dotted line indicates unity; the continuous line is the result of a fit to Eq. 1.

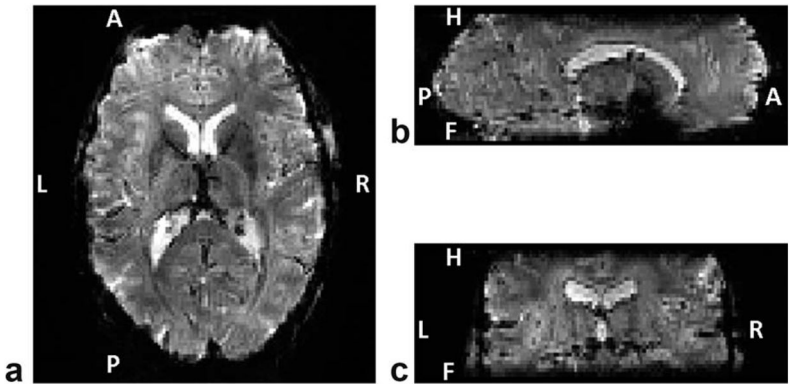

FIG. 2.

Example slices taken from a human data set with a spatial resolution of 1.5*1.5*2 mm and 32 segments. **a:** transverse, (**b**) sagittal, and (**c**) coronal planes. Note the presence of signal in the frontal lobe area. The image was bias-field corrected for presentation.

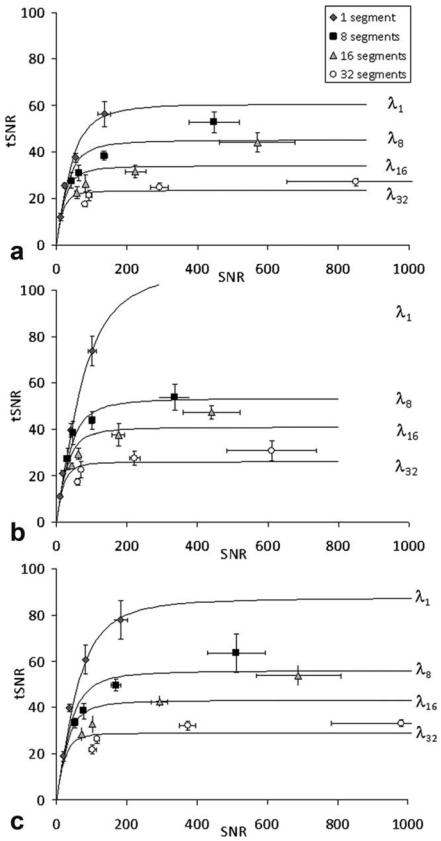

FIG. 3.

tSNR versus SNR_0 *in-vivo* in (**a**) grey matter, (**b**) white matter and (**c**) CSF for data acquired with 1, 8, 16, or 32 segments. Each data series contains four measurement points with increasing SNR_0 from data acquired with in-plane resolutions of 1.5, 2, 3, and 5 mm, respectively. The error bars indicate the standard error over subjects (5). The results of a nonlinear least squares fit to Eq. 1 are shown as continuous lines.

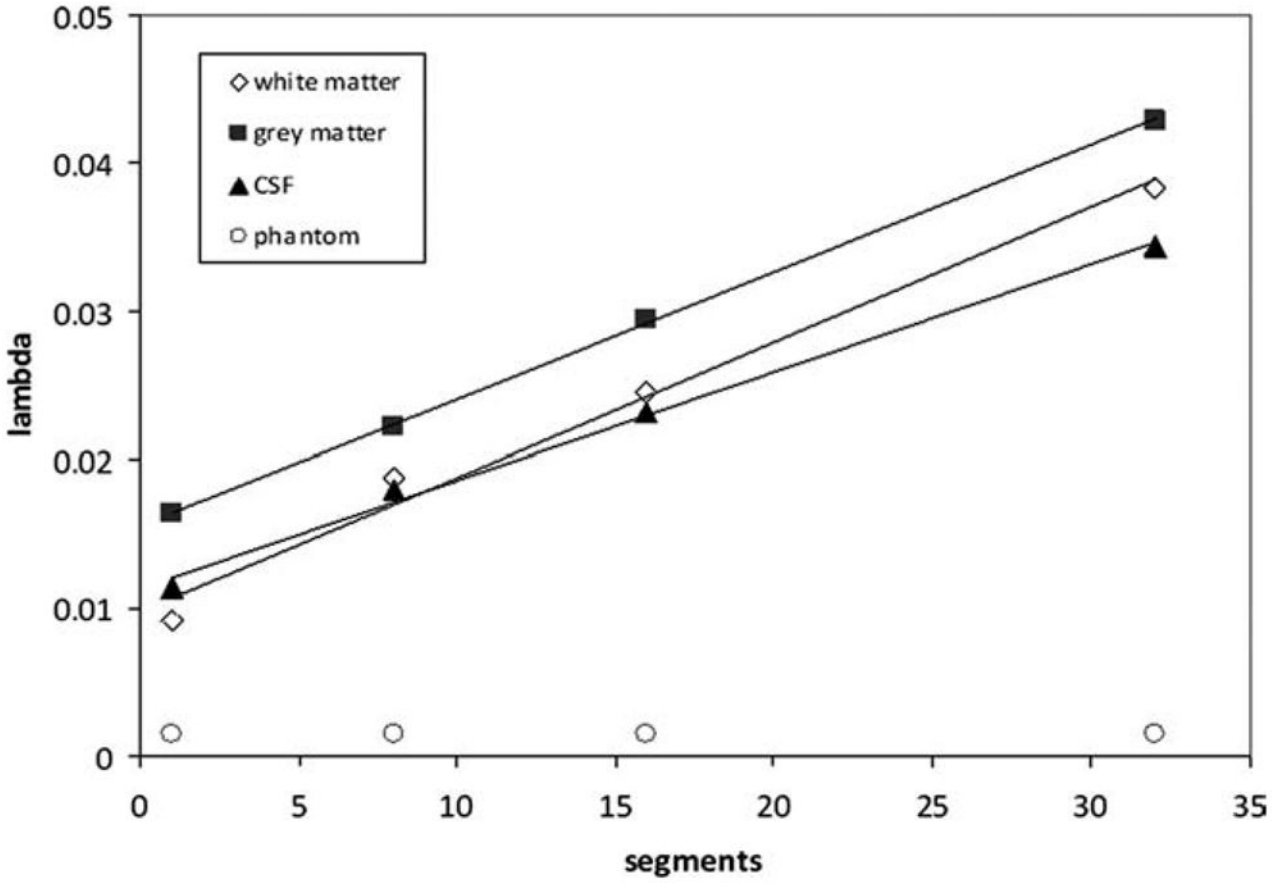

FIG. 4.

λ versus number of segments in grey matter, white matter and CSF. Note that higher values for λ result in lower $tSNR_{max}$ values. $\lambda_{phantom}$ are shown for reference. The result of a linear regression of λ values versus number of segments is shown overlaid for each tissue type. The slope of the regression was 0.0009, 0.0009, and 0.0007 for grey matter, white matter and CSF, respectively.

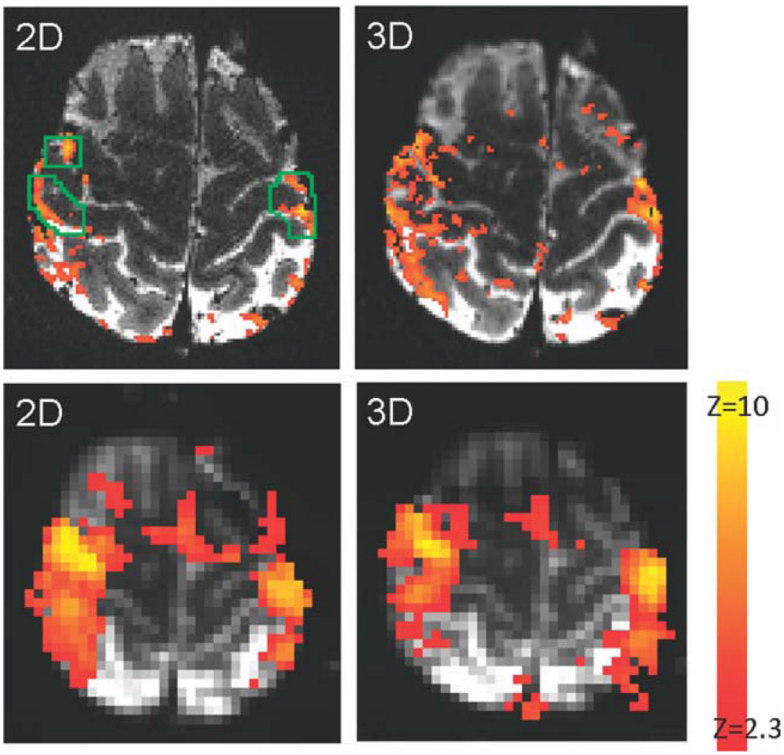

FIG. 5.

Activation maps from a single subject for the finger-tapping task. Maps from data acquired with 2D-EPI are shown on the left and maps acquired with 3D-EPI are shown on the right. 1mm data are shown on the top row, 3mm data on the bottom row. The scaling of the activation maps is the same in all cases. The activation maps are shown overlaid on a, coregistered, 2D-echo planar image, which had good CSF-white matter contrast. The ROI over which mean z-scores were measured is shown overlaid on the 1mm 2D-EPI activation map.

Table 1

Acquisition Parameters

	8 channel coil; phantom and human experiments			CP coil; phantom experiments		
Segments	**Resolution**	**Matrix size**	**Acq time**	**Resolution**	**Matrix size**	**Acq time**
1	1.5 × 1.5	128 × 128	7.5 s	2 × 2 × 2	96 × 96	7.5 s
1	2 × 2	96 × 96	7.5 s	3 × 3 × 2	96 × 96	7.5 s
1	3 × 3	96 × 96	7.5 s	4 × 4 × 2	96 × 96	7.5 s
1	5 × 5	96 × 96	7.5 s	5 × 5 × 2	96 × 96	7.5 s
1				5 × 5 × 5	96 × 96	7.5 s
1				5 × 5 × 8	96 × 96	7.5 s
8	1.5 × 1.5	128 × 128	60 s	2 × 2 × 2	96 × 96	60 s
8	2 × 2	96 × 96	60 s	3 × 3 × 2	96 × 96	60 s
8	3 × 3	96 × 96	60 s	4 × 4 × 2	96 × 96	60 s
8	5 × 5	96 × 96	60 s	5 × 5 × 2	96 × 96	60 s
8				5 × 5 × 5	96 × 96	60 s
16	1.5 × 1.5	128 × 128	120 s	2 × 2 × 2	96 × 96	120 s
16	2 × 2	96 × 96	120 s	3 × 3 × 2	96 × 96	120 s
16	3 × 3	96 × 96	120 s	4 × 4 × 2	96 × 96	120 s
16	5 × 5	96 × 96	120 s	5 × 5 × 2	96 × 96	120 s
32	1.5 × 1.5	128 × 128	240 s	2 × 2 × 2	96 × 96	240 s
32	2 × 2	96 × 96	240 s	3 × 3 × 2	96 × 96	240 s
32	3 × 3	96 × 96	240 s	4 × 4 × 2	96 × 96	240 s
32	5 × 5	96 × 96	240 s	5 × 5 × 2	96 × 96	240 s

Table 2

Values of λ Obtained From Fitting Individual Subject Data (Columns 1–5) and the Subject Means (Column 6)

Subject	Segments	1	2	3	4	5	Average
Grey matter	1	0.018	0.008	0.018	0.023	0.013	0.016 ± 0.003
	8	0.014	0.022	0.029	0.027	0.022	0.022 ± 0.007
	16	0.019	0.045	0.031	0.024	0.020	0.029 ± 0.012
	32	0.031	0.063	0.042	0.045	0.043	0.043 ± 0.011 *
White matter	1	0.014	0.000	0.013	0.011	0.007	0.009 ± 0.003
	8	0.016	0.017	0.026	0.016	0.019	0.019 ± 0.003 *
	16	0.023	0.032	0.027	0.024	0.025	0.024 ± 0.007 *
	32	0.037	0.062	0.043	0.028	0.035	0.038 ± 0.013 *
CSF	1	0.011	0.005	0.016	0.016	0.010	0.011 ± 0.002
	8	0.009	0.016	0.027	0.026	0.021	0.018 ± 0.005 *
	16	0.012	0.032	0.028	0.034	0.024	0.023 ± 0.009 *
	32	0.020	0.044	0.037	0.041	0.042	0.034 ± 0.009 *

For the subject means, the 95% confidence interval is given.

* indicates a significant difference with the λ obtained for the 1-segment acquisition (two-tailed *t*-test, $P < 0.05$)